ARTICLE

https://doi.org/10.1038/s41586-018-0105-3

Reconstitution reveals motor activation for intraflagellar transport

Mohamed A. A. Mohamed[1], Willi L. Stepp[1] & Zeynep Ökten[1,2]*

The human body represents a notable example of ciliary diversification. Extending from the surface of most cells, cilia accomplish a diverse set of tasks. Predictably, mutations in ciliary genes cause a wide range of human diseases such as male infertility and blindness. In *Caenorhabditis elegans* sensory cilia, this functional diversity appears to be traceable to the differential regulation of the kinesin-2-powered intraflagellar-transport (IFT) machinery. Here we reconstituted the first, to our knowledge, functional multi-component IFT complex that is deployed in the sensory cilia of *C. elegans*. Our bottom-up approach revealed the molecular basis of specific motor recruitment to the IFT trains. We identified the key component that incorporates homodimeric kinesin-2 into its physiologically relevant context, which in turn allosterically activates the motor for efficient transport. These results will enable the molecular delineation of IFT regulation, which has eluded understanding since its discovery more than two decades ago.

Having been neglected for decades, the biology of cilia underwent a renaissance after the realization that ciliogenesis is central to development and disease[1–5]. Almost all cilia are built by the highly conserved IFT machinery with a few exceptions in which cilia are built in the cytoplasm in an IFT-independent manner[5–8]. Numerous in vivo studies have established the universal characteristics of IFT in diverse model systems. The IFT trains display continuous movement towards either the ciliary tip (kinesin-2-dependent) or the ciliary base (dynein-2-dependent) without apparent reversals in between[5,7,9–11]. When a kinesin-2-powered IFT train arrives at the ciliary tip, it undergoes a poorly understood remodelling process that deactivates the kinesin-2 motor and restructures the train for dynein-2-dependent transport back to the base[5,7,9–11]. It has long been known that *C. elegans* uses two different kinesin motors, a heterotrimeric kinesin-2 called kinesin-II and a homodimeric kinesin-2 called OSM-3, to build its functionally distinct cilia[12]. Loss of the homodimeric OSM-3 function invariably leads to the loss of the distal portion of the canonical cilium and to deficient osmotic avoidance in the so-called rod-shaped or 'canonical' cilia, whereas the loss of both the heterotrimeric and homodimeric kinesin-2 motors leads to the loss of entire axonemes[12]. In the wing-shaped AWC cilia, on the other hand, loss of the heterotrimeric kinesin-2 motor leads to deficiencies in chemotaxis, suggesting that the kinesin-dependent trafficking of cilia-specific components defines the functional identity of the respective cilia[13,14]. In contrast to the heterotrimeric kinesin-2, the precise role of the homodimeric kinesin-2 in other organisms is much less understood[7]. For instance, the homodimeric kinesin-2 moves along the mammalian cilia, but it has not yet been shown to function as an IFT motor[15,16].

Despite its essential role in ciliogenesis and its emerging role in ciliary diversity[13,14,17–19], the mechanisms of IFT train assembly, motor recruitment, and the timely activation and deactivation of the oppositely directed kinesin-2 and dynein-2 motors are poorly understood. To move towards a comprehensive molecular understanding of IFT, here we used a bottom-up approach to dissect the OSM-3-dependent IFT in *C. elegans* sensory cilia. The OSM-3 function was previously linked to the so-called IFT-B complex[20]. Loss of function in many IFT-B subunits has been proposed to interfere with OSM-3 function in vivo, and many of these subunits have been shown to be part of the IFT-B core complex[20–24] (Extended Data Fig. 1). Previous work with the green algae *Chlamydomonas reinhardtii* was instrumental to the detailed characterization of the IFT components. The entire IFT-B complex consisting of the peripheral and core complexes has been reconstituted from 15 recombinantly expressed subunits[25]. Specifically, nine core components (IFT-74, IFT-81, IFT-27, IFT-25, IFT-22, IFT-52, IFT-46, IFT-88 and IFT-70) form a stable complex; several of these core components can also combine autonomously to form sub-complexes in vitro[26–29]. Guided by these previous findings, we concentrated on the IFT-B core complex and started our bottom-up approach by first assembling the presumptive sub-complexes using recombinantly expressed wild-type, full-length subunits from *C. elegans*. Next, we systematically probed the interaction of the sub-complexes, as well as their individual subunits, with the OSM-3 motor using multiple techniques. To visualize the motor activity in functional-transport assays, we used a previously described, constitutively active OSM-3(G444E) motor[30] that we C-terminally tagged for fluorophore labelling using the HaloTag system (hereafter the tagged motor is referred to as OSM-3(G444E)–Halo).

Building the first IFT–kinesin-2 complex

To monitor complex formation, we made use of size-exclusion chromatography that was coupled to multiple-angle light scattering (SEC–MALS) analysis to gauge the molecular mass of the presumptive complexes. We first assessed whether the tripartite IFT-74–IFT-81–IFT-22(IFTA-2) (symbols in parentheses refer to the *C. elegans* protein nomenclature) core complex (hereafter TCC; blue subunits in Extended Data Fig. 1), and the quadripartite IFT-52(OSM-6)–IFT-46(DYF-6)–IFT-88(OSM-5)–IFT-70(DYF-1) core complex (hereafter QCC; magenta subunits in Extended Data Fig. 1) are formed stably or whether additional factors were necessary (that is, IFT-27 and IFT-25 subunits that are present in the IFT-B core complex of *C. reinhardtii* but not in *C. elegans*[29]). Although both complexes were formed, only the QCC, and not the TCC, incorporated the motor protein (Fig. 1 and Extended Data Fig. 2a–c). Notably, removal of the IFT-70(DYF-1) subunit from the QCC disrupted the complex formation between the motor and its IFT-B complex, suggesting an IFT-70(DYF-1)-specific recruitment of the motor (Fig. 1, middle versus right). Consistent with this notion, the motor was found under the elution peak with QCC

---

[1]Physik Department E22, Technische Universität München, Garching, Germany. [2]Munich Center for Integrated Protein Science, Munich, Germany. *e-mail: zoekten@ph.tum.de

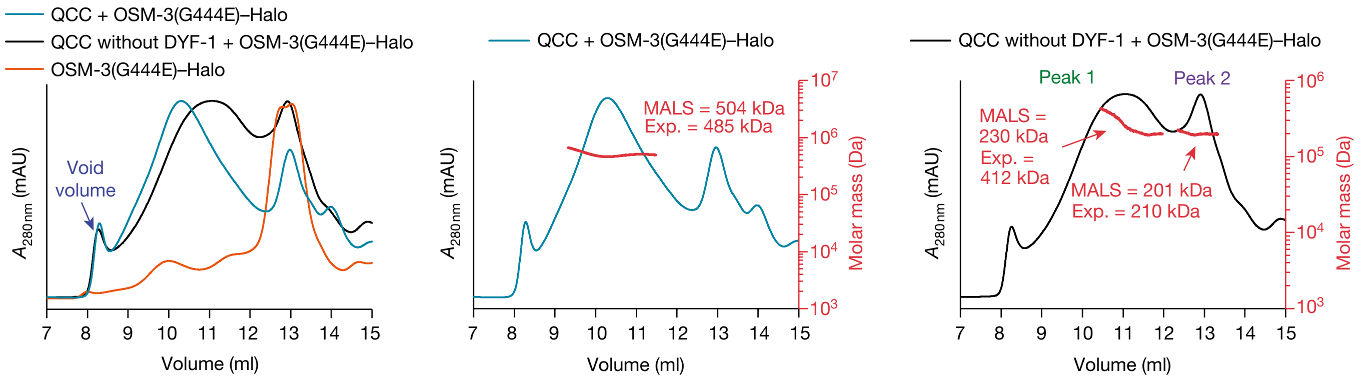

Fig. 1 | IFT-70(DYF-1) is key to the incorporation of the OSM-3 motor into the QCC. Overlay of the elution profiles of QCC lacking IFT-70(DYF-1) (labelled as QCC without DYF-1) + OSM-3(G444E)–Halo and QCC + OSM-3(G444E)–Halo along with the OSM-3(G444E)–Halo motor show the IFT-70(DYF-1)-dependent shift of the elution peaks upon incorporation of the motor into the QCC (left). The MALS analyses of the complexes are also shown (middle and right). The molar mass determined from the MALS fit and the expected mass (Exp.) of the complexes are shown in red (right axes and insets). Results are representative of three independent experiments.

and was absent under QCC peak when the IFT-70(DYF-1) subunit was removed (Extended Data Fig. 2a, middle versus right).

To provide independent biochemical evidence for the IFT-70(DYF-1)-mediated interaction of the motor with the QCC, we turned to in-solution protein-binding assays. Using microscale thermophoresis (MST), we observed robust, sub-micromolar binding of the motor protein to the QCC, whereas removal of the IFT-70(DYF-1) subunit abolished this interaction (Fig. 2). Taken together, our solution-based SEC–MALS and MST analyses demonstrate the specific, IFT-70(DYF-1)-mediated recruitment of the OSM-3 motor to the IFT-B complex.

To further corroborate the key role of the IFT-70(DYF-1) subunit in OSM-3 recruitment, we next turned to fluorescence-based microscopy assays. We functionalized each of the IFT-B subunits with different fluorescent tags and then performed photobleaching assays that detected non-aggregated single subunits (Extended Data Fig. 3). Next, we determined the pairwise colocalization efficiencies by labelling the respective subunits with two different fluorophores. This exclusion process demonstrated that the functionalized subunits retained their capability to assemble into a stable complex under assay conditions (Extended Data Fig. 4). To find out which of these sub-complexes display efficient colocalization with the motor, we differentially labelled OSM-3(G444E)–Halo and each of the sub-complexes. Consistent with our previous assays that demonstrated the IFT-70(DYF-1)-dependent interaction between the motor and its IFT-B complex (Figs. 1, 2), OSM-3(G444E)–Halo failed to colocalize efficiently with TCCs and QCCs that lacked IFT-70(DYF-1), but displayed significant colocalization with the QCC that contained the IFT-70(DYF-1) subunit (Fig. 3a). Finally, the efficient colocalization of the IFT-70(DYF-1) subunit with OSM-3(G444E)–Halo, which did not occur with IFT-52(OSM-6), IFT-88(OSM-5) or IFT-46(DYF-6) subunits, provided direct evidence that IFT-70(DYF-1) is the key subunit that mediates the interaction between the motor and the IFT-B core complex (Fig. 3b). By contrast, the heterotrimeric KLP11–KLP20–KAP motor, which cooperates with OSM-3 to build the rod-shaped sensory cilium in *C. elegans*, failed to colocalize with the IFT-B complex (Extended Data Fig. 5). Previous in vivo experiments suggested that the KLP11–KLP20–KAP motor associates with the IFT-A complex[20].

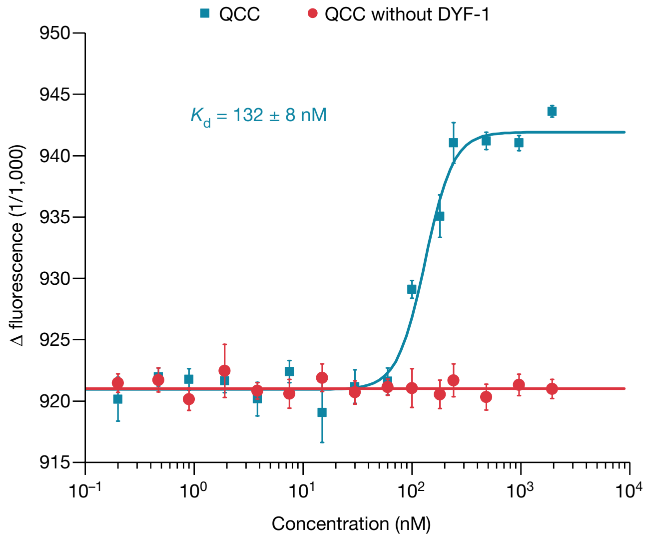

Fig. 2 | IFT-70(DYF-1)-mediated binding of the OSM-3(G444E)–Halo motor to the QCC as measured by MST. The fluorophore-labelled motor was titrated with both the QCC and QCC lacking IFT-70(DYF-1). Data are mean ± s.d. from three independent experiments. Source Data are provided with the online version the paper.

Functional transport assays arguably provide the most direct evidence for the specific recruitment and activation of the OSM-3 motor by the IFT-70(DYF-1) subunit. To assess whether our reconstituted OSM-3–IFT-B complex is capable of directional movement in vitro, we tracked the differentially fluorophore-labelled OSM-3(G444E)–Halo motor and its IFT-B complex using a total internal reflection fluorescence (TIRF) microscope. Most of the fluorophore signals from the motor and its complex were colocalized and moved directionally on surface-attached microtubules (Fig. 4a and Supplementary Video 1). Consistent with our previous assays, removal of IFT-70(DYF-1) again terminated the interaction between the motor with QCC, and the OSM-3(G444E)–Halo motor moved alone along microtubules (Supplementary Video 1). Notably, incorporation of the motor into the QCC further enhanced the velocity of OSM-3(G444E)–Halo, whereas the velocities of the motor alone or in the presence of the IFT-70(DYF-1) subunit were indistinguishable (Fig. 4a). The processivity of the respective motors, by contrast, was independent of the IFT-70(DYF-1) subunit or the QCC (Extended Data Fig. 6a).

The point mutation in the stalk of the OSM-3(G444E)–Halo construct hampers the auto-inhibitory folding, which in turn results in an activated motor in vitro[30]. Therefore, we next asked whether the IFT-70(DYF-1) subunit can also activate the auto-inhibited OSM-3 motor in our reconstitution assays. We designed a motor with a wild-type stalk that lacked the G444E mutation. We introduced an N-terminal Flag and a SNAP-tag for affinity purification and fluorophore labelling of the motor (hereafter OSM-3–SNAP), respectively. In this construct, the entire C terminus that follows the catalytic heads was not modified. As demonstrated with OSM-3(G444E)–Halo (Fig. 3), the OSM-3–SNAP motor with an unmodified C terminus displayed efficient IFT-70(DYF-1)-dependent colocalization with the QCC, but

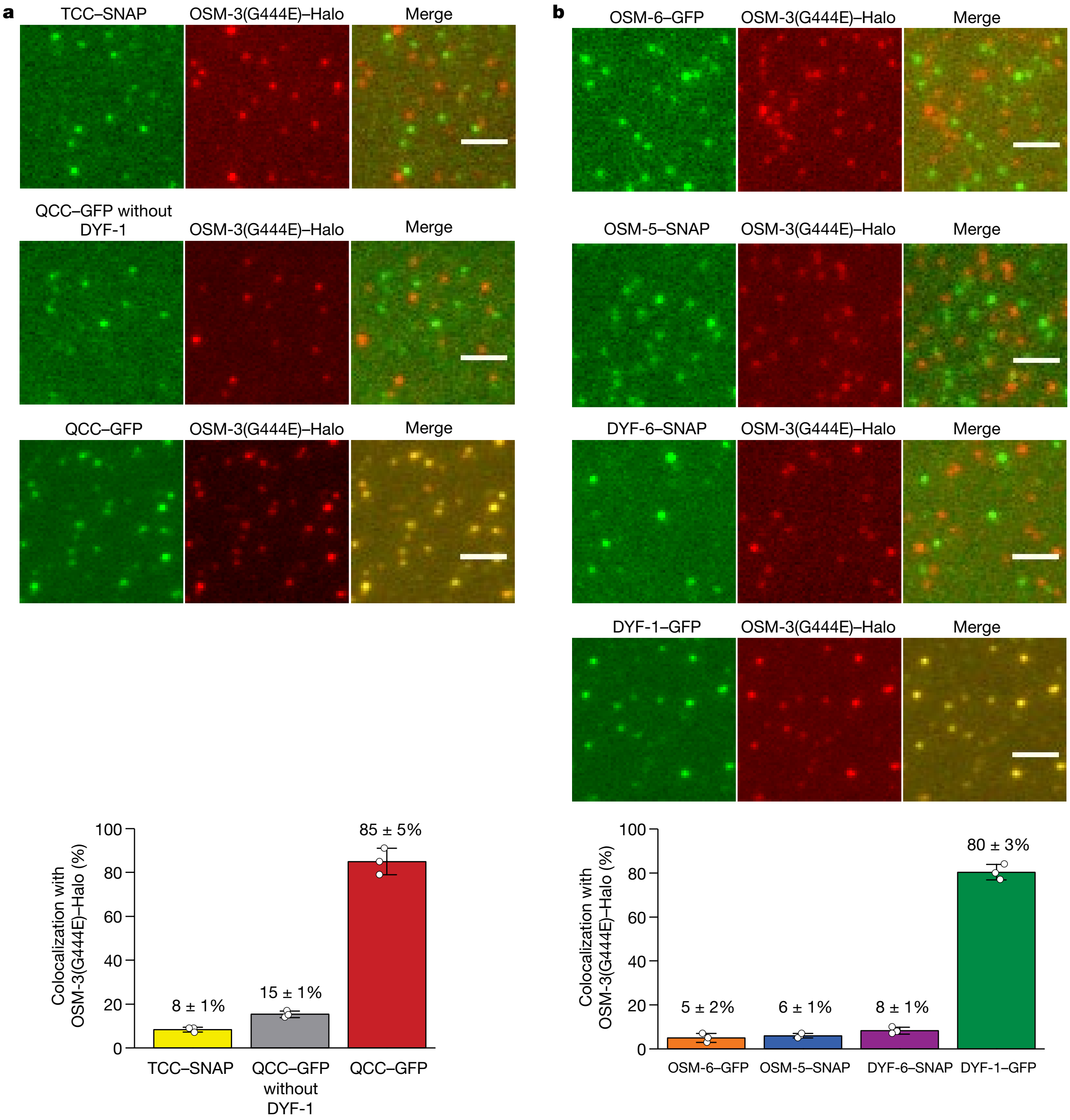

Fig. 3 | Colocalization efficiency of the OSM-3(G444E)–Halo motor with its IFT-B complex is solely dependent on the IFT-70(DYF-1) subunit. a, Neither TCC nor QCC that lacked IFT70(DYF-1) displayed efficient colocalization with the OSM-3(G444E)–Halo motor. In the presence of the IFT-70(DYF-1) subunit, however, the QCC efficiently colocalized with OSM-3(G444E)–Halo (85 ± 5%). **b**, Consistently, OSM-3(G444E)–Halo failed to interact with individual IFT-52(OSM-6), IFT-88(OSM-5) and IFT-46(DYF-6) subunits but showed robust colocalization (80 ± 3%) with the IFT-70(DYF-1) subunit. IFT-81 and IFT-52(OSM-6) were fluorescently labelled with C-terminal SNAP and green fluorescent protein (GFP) tags, respectively. Data are mean ± s.d. from three independent experiments. Source Data are available with the online version of the paper. Scale bars, 3 μm.

not with the TCC (Extended Data Fig. 7a). OSM-3–SNAP interacted with the IFT-70(DYF-1) subunit but not with the IFT-52(OSM-6), IFT-88(OSM-5) or IFT-46(DYF-6) subunits (Extended Data Fig. 7b). However, the auto-regulation in kinesin motors is achieved by folding of the distal tail domain at the C terminus onto the N-terminal head domains[30]. To ensure that the N-terminal SNAP-tag does not impede the auto-inhibitory folding of the motor, we also designed a construct that was only Flag-tagged at its C terminus for affinity purification (hereafter OSM-3–Flag). Owing to the lack of fluorescence information, this motor cannot be followed directly in the functional transport assays; however, it represents the wild-type OSM-3 as closely as possible. Both motors containing the wild-type stalk were recruited and activated in an IFT-70(DYF-1)-specific manner (Fig. 4b, c and Supplementary Videos 2, 3). The IFT-70(DYF-1)-dependent activation was much more obvious with the OSM-3–SNAP motor that lacked the G444E mutation. As expected from an auto-inhibited kinesin, and in stark contrast to the OSM-3(G444E)–Halo motor, OSM-3–SNAP (which has a wild-type stalk) was barely capable of directional movement but rather displayed two-dimensional diffusion (compare the top left of Supplementary Video 1 to the top left of Supplementary Video 2). The presence of IFT-70(DYF-1) or the QCC initiated robust directional movement of the auto-inhibited OSM-3–SNAP motor (Supplementary Video 2). Finally—as with the OSM-3(G444E)–Halo motor (Extended Data Fig. 6a)—once activated by IFT-70(DYF-1), the processivity of OSM-3–SNAP and OSM-3–Flag motors was not modified by the presence of IFT-70(DYF-1) alone or the QCC (Extended Data Fig. 6b, c).

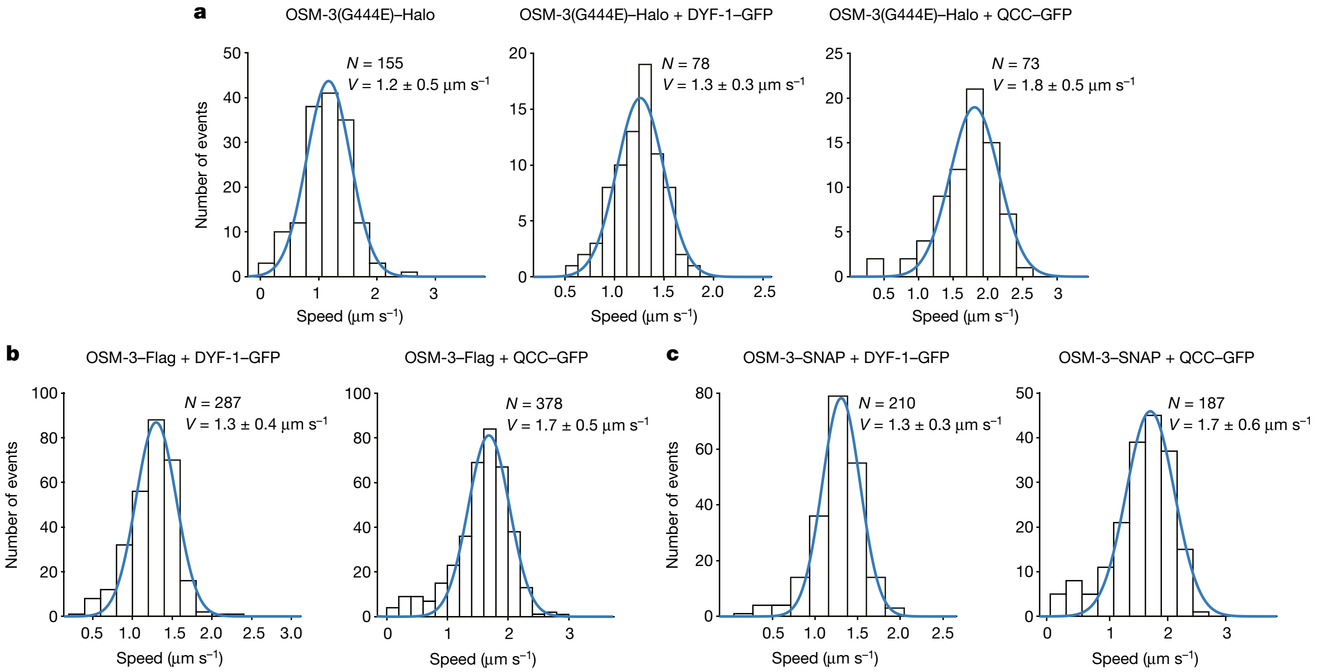

Fig. 4 | IFT-70(DYF-1)-dependent incorporation into the QCC fully activates OSM-3 in vitro. a, In the presence (middle) and absence (left) of IFT-70(DYF-1), the velocity (V) of OSM-3(G444E)–Halo is indistinguishable but incorporation into the QCC (right) significantly increases the velocity of the motor. P values from a two-tailed t-test assuming unequal variances: OSM-3(G444E)–Halo versus OSM-3(G444E)–Halo + DYF-1–GFP, 0.013; OSM-3(G444E)–Halo versus OSM-3(G444E)–Halo + QCC–GFP, 2.5×10^{-18}; OSM-3(G444E)–Halo + DYF-1–GFP versus OSM-3(G444E)–Halo + QCC–GFP, 3.4×10^{-15}. **b**, **c**, Consistently, QCC fully activates the OSM-3–Flag (**b**, $P = 9.6 \times 10^{-25}$) and OSM-3–SNAP (**c**, $P = 1.8 \times 10^{-12}$) complexes but not the IFT-70(DYF-1) subunit alone. N, number of events obtained from three different flow chambers in three independent experiments (velocities fit to a Gaussian distribution, mean ± s.d.).

Taken together, our functional transport assays consistently showed that the presence of IFT-70(DYF-1) is essential for the recruitment of the OSM-3 motor to the IFT-B complex. Our results further revealed that the presence of the IFT-70(DYF-1) subunit alone is not sufficient to fully activate the motor. Instead, it is the IFT-70(DYF-1)-mediated incorporation of OSM-3 into the IFT-B complex that allosterically activates the motor. Notably, the transport rates extracted from our in vitro reconstitution assays were consistent with rates extracted from in vivo studies[12,20,31]. The physiological relevance of our reconstitution is underscored by previous in vivo findings in the *C. elegans* sensory cilium. In the absence of *dyf-1* function, OSM-3 not only appeared to detach from the IFT trains, it also failed to move directionally but diffused along the cilium instead[20] (see Supplementary Video 2, top left). This finding can now be explained by the direct role of the IFT-70(DYF-1) subunit in specific motor recruitment and activation as shown in this study. These results represent a functional reciprocity that is particularly notable given the complexity of the IFT machinery. Our work directly demonstrates the molecular mechanism by which an IFT motor is recruited to its IFT train, and is an example of the power of bottom-up approaches to delineate the underlying mechanisms of highly convoluted processes such as ciliogenesis.

Online content

Any Methods, including any statements of data availability and Nature Research reporting summaries, along with any additional references and Source Data files, are available in the online version of the paper at https://doi.org/10.1038/s41586-018-0105-3.

Received: 2 November 2017; Accepted: 23 March 2018;
Published online 9 May 2018.

1. Sharma, N., Berbari, N. F. & Yoder, B. K. Ciliary dysfunction in developmental abnormalities and diseases. *Curr. Top. Dev. Biol.* **85**, 371–427 (2008).
2. Pazour, G. J. & Rosenbaum, J. L. Intraflagellar transport and cilia-dependent diseases. *Trends Cell Biol.* **12**, 551–555 (2002).
3. Marshall, W. F. The cell biological basis of ciliary disease. *J. Cell Biol.* **180**, 17–21 (2008).
4. Goetz, S. C. & Anderson, K. V. The primary cilium: a signalling centre during vertebrate development. *Nat. Rev. Genet.* **11**, 331–344 (2010).
5. Pedersen, L. B. & Rosenbaum, J. L. Intraflagellar transport (IFT) role in ciliary assembly, resorption and signalling. *Curr. Top. Dev. Biol.* **85**, 23–61 (2008).
6. Kozminski, K. G., Johnson, K. A., Forscher, P. & Rosenbaum, J. L. A motility in the eukaryotic flagellum unrelated to flagellar beating. *Proc. Natl Acad. Sci. USA* **90**, 5519–5523 (1993).
7. Prevo, B., Scholey, J. M. & Peterman, E. J. G. Intraflagellar transport: mechanisms of motor action, cooperation, and cargo delivery. *FEBS J.* **284**, 2905–2931 (2017).
8. Avidor-Reiss, T. & Leroux, M. R. Shared and distinct mechanisms of compartmentalized and cytosolic ciliogenesis. *Curr. Biol.* **25**, R1143–R1150 (2015).
9. Scholey, J. M. Intraflagellar transport. *Annu. Rev. Cell Dev. Biol.* **19**, 423–443 (2003).
10. Rosenbaum, J. L. & Witman, G. B. Intraflagellar transport. *Nat. Rev. Mol. Cell Biol.* **3**, 813–825 (2002).
11. Taschner, M. & Lorentzen, E. The intraflagellar transport machinery. *Cold Spring Harb. Perspect. Biol.* **8**, a028092 (2016).
12. Snow, J. J. et al. Two anterograde intraflagellar transport motors cooperate to build sensory cilia on *C. elegans* neurons. *Nat. Cell Biol.* **6**, 1109–1113 (2004).
13. Mukhopadhyay, S. et al. Distinct IFT mechanisms contribute to the generation of ciliary structural diversity in *C. elegans*. *EMBO J.* **26**, 2966–2980 (2007).
14. Evans, J. E. et al. Functional modulation of IFT kinesins extends the sensory repertoire of ciliated neurons in *Caenorhabditis elegans*. *J. Cell Biol.* **172**, 663–669 (2006).
15. Jenkins, P. M. et al. Ciliary targeting of olfactory CNG channels requires the CNGB1b subunit and the kinesin-2 motor protein, KIF17. *Curr. Biol.* **16**, 1211–1216 (2006).
16. Leaf, A. & Von Zastrow, M. Dopamine receptors reveal an essential role of IFT-B, KIF17, and Rab23 in delivering specific receptors to primary cilia. *eLife* **4**, e06996 (2015).
17. Silverman, M. A. & Leroux, M. R. Intraflagellar transport and the generation of dynamic, structurally and functionally diverse cilia. *Trends Cell Biol.* **19**, 306–316 (2009).
18. Bae, Y. K. & Barr, M. M. Sensory roles of neuronal cilia: cilia development, morphogenesis, and function in *C. elegans*. *Front. Biosci.* **13**, 5959–5974 (2008).
19. Bae, Y. K. et al. General and cell-type specific mechanisms target TRPP2/PKD-2 to cilia. *Development* **133**, 3859–3870 (2006).
20. Ou, G., Blacque, O. E., Snow, J. J., Leroux, M. R. & Scholey, J. M. Functional coordination of intraflagellar transport motors. *Nature* **436**, 583–587 (2005).
21. Hao, L. et al. Intraflagellar transport delivers tubulin isotypes to sensory cilium middle and distal segments. *Nat. Cell Biol.* **13**, 790–798 (2011).

22. Ou, G. et al. Sensory ciliogenesis in *Caenorhabditis elegans*: assignment of IFT components into distinct modules based on transport and phenotypic profiles. *Mol. Biol. Cell* **18**, 1554–1569 (2007).
23. Burghoorn, J. et al. Mutation of the MAP kinase DYF-5 affects docking and undocking of kinesin-2 motors and reduces their speed in the cilia of *Caenorhabditis elegans*. *Proc. Natl Acad. Sci. USA* **104**, 7157–7162 (2007).
24. Masyukova, S. V. et al. A screen for modifiers of cilia phenotypes reveals novel MKS alleles and uncovers a specific genetic interaction between *osm-3* and *nphp-4*. *PLoS Genet.* **12**, e1005841 (2016).
25. Taschner, M. et al. Intraflagellar transport proteins 172, 80, 57, 54, 38, and 20 form a stable tubulin-binding IFT-B2 complex. *EMBO J.* **35**, 773–790 (2016).
26. Taschner, M., Bhogaraju, S. & Lorentzen, E. Architecture and function of IFT complex proteins in ciliogenesis. *Differentiation* **83**, S12–S22 (2012).
27. Piperno, G. & Mead, K. Transport of a novel complex in the cytoplasmic matrix of *Chlamydomonas* flagella. *Proc. Natl Acad. Sci. USA* **94**, 4457–4462 (1997).
28. Cole, D. G. et al. *Chlamydomonas* kinesin-II-dependent intraflagellar transport (IFT): IFT particles contain proteins required for ciliary assembly in *Caenorhabditis elegans* sensory neurons. *J. Cell Biol.* **141**, 993–1008 (1998).
29. Taschner, M., Bhogaraju, S., Vetter, M., Morawetz, M. & Lorentzen, E. Biochemical mapping of interactions within the intraflagellar transport (IFT) B core complex: IFT52 binds directly to four other IFT-B subunits. *J. Biol. Chem.* **286**, 26344–26352 (2011).
30. Imanishi, M., Endres, N. F., Gennerich, A. & Vale, R. D. Autoinhibition regulates the motility of the *C. elegans* intraflagellar transport motor OSM-3. *J. Cell Biol.* **174**, 931–937 (2006).
31. Prevo, B., Mangeol, P., Oswald, F., Scholey, J. M. & Peterman, E. J. Functional differentiation of cooperating kinesin-2 motors orchestrates cargo import and transport in *C. elegans* cilia. *Nat. Cell Biol.* **17**, 1536–1545 (2015).

Acknowledgements We thank G. Woehlke, E. J. G. Peterman, E. Lorentzen, M. Taschner and F. Müller-Planitz for discussions throughout this work, T.-H. Ho for technical assistance and A. Oberhofer and F. Müller-Planitz for critically reading the manuscript. This work was supported by European Research Council Grant 335623 (to Z.Ö.). We apologize to our colleagues whose work could not be cited owing to space limitations.

Reviewer information *Nature* thanks R. Vale and the other anonymous reviewer(s) for their contribution to the peer review of this work.

Author contributions M.A.A.M. and Z.Ö. designed the experiments. M.A.A.M. performed the experiments and analysed the data. W.L.S. wrote all the customized MATLAB routines. Z.Ö. and M.A.A.M. wrote the manuscript.

Competing interests The authors declare no competing interests.

Additional information

Extended data is available for this paper at https://doi.org/10.1038/s41586-018-0105-3.
Supplementary information is available for this paper at https://doi.org/10.1038/s41586-018-0105-3.
Reprints and permissions information is available at http://www.nature.com/reprints.
Correspondence and requests for materials should be addressed to Z.Ö.

METHODS

No statistical methods were used to predetermine sample size. The experiments were not randomized and the investigators were not blinded to allocation during experiments and outcome assessment.

DNA and protein constructs. All DNA constructs used in this study were commercially synthesized (GenScript), they were based on sequence information that is available from the WormBase (http://www.wormbase.org) and cloned into the pFastBac1 vector according to the manufacturer's instructions (Thermo Fisher). In addition, the pFastBac1 vector was functionalized with Halo, SNAP, or GFP genes for C-terminal tagging of several constructs as described in the manuscript. Three different OSM-3 constructs were designed for this study (see Supplementary Information for details of DNA and protein sequences).

Protein expression, purification and fluorescent labelling. The Baculovirus Expression System (Thermo Fisher) was used to express all proteins in insect cells (Sf9) according to the manufacturer's instructions.

For protein purification, Sf9 cells at a concentration of 2×10^6 cells ml^{-1} were infected with the corresponding viruses. After 65 h of incubation at 28 °C, the cells were collected by centrifugation for 15 min at 2,600*g*. Cell pellets were lysed in PIPES buffer (50 mM PIPES, pH 6.9, 300 mM potassium acetate, 1 mM $MgCl_2$, 1 mM dithiothreitol (DTT), 0.5% Triton X-100, 10% glycerol, 0.1 mM ATP, Complete Protease Inhibitor Cocktail (Roche)). Lysed cells were pelleted by centrifugation for 10 min at 40,000*g*. The supernatant was incubated with 60 μl of Anti-Flag M2 Affinity Gel (Sigma) for 90 min. The Flag-resin was washed three times with 1 ml of wash buffer 1 (80 mM PIPES, pH 6.9, 500 mM potassium acetate, 1 mM $MgCl_2$, 1 mM DTT, 5 μM ATP, 10% glycerol, 0.1% Tween-20, 1 mM EGTA) and three times with 1 ml of wash buffer 2 (80 mM PIPES, pH 6.9, 200 mM potassium acetate, 1 mM $MgCl_2$, 1 mM DTT, 0.1 mM ATP, 10% glycerol, 0.1% Tween-20, 1 mM EGTA). The Flag resin was incubated in a rotator for 30 min at room temperature with 150 μl wash buffer 2 containing either 1 mM HaloTag Alexa Fluor660 ligand (for labelling OSM-3(G444E)–Halo) or 1 mM SNAP-Surface Alexa Fluor 647 or 488 (for labelling OSM-3–SNAP and the corresponding IFT-B subunits). The Flag resin was washed three times with 1 ml of wash buffer 2 and eluted with 70 μl of elution buffer (wash buffer 2 containing 0.5 mg ml^{-1} of 1 × Flag Peptide (Sigma)) for 60 min at 4 °C[32,33].

SEC–MALS. SEC–MALS analyses were used to determine the absolute molar masses of the protein complexes. The TSKgel G4000SW$_{XL}$ (Tosoh Biosciences) and the Superose 6 Increase 10/300 GL columns (GE Healthcare) were calibrated with at least two column volumes of the gel filtration buffer (25 mM PIPES, pH 7.0, 200 mM NaCl, 1 mM $MgCl_2$, 1 mM EGTA, 1 mM DTT). The columns were inline with a variable UV-absorbance detector (Agilent 1260 Infinity series) and a DAWN8 + MALS detector (Wyatt Technology). Molar masses were calculated with ASTRA 6 software (Wyatt Technology) with the d*n*/d*c* value set to 0.185 ml g^{-1}. Bovine serum albumin (BSA) was used as a calibration standard.

MST assay. OSM-3(G444E)–Halo interaction with either the QCC or the QCC lacking IFT70(DYF-1) was measured using MST with a Monolith NT.115 (NanoTemper Technologies GmbH). The fluorophore-labelled OSM-3(G444E)–Halo at 10 nM was titrated with the respective (unlabelled) binding partner, the concentration of which varied between 0.2 nM and 2 μM in the MST buffer (50 mM Tris-HCl (pH 7.6), 150 mM NaCl, 1 mM $MgCl_2$, 0.1% Tween 20, 1 mM EGTA, 1 mM DTT, 10% glycerol). Standard coated capillaries were used in all measurements. K_d values were determined using NanoTemper Analysis software.

Photobleaching experiments and single-molecule assays. Photobleaching experiments and single-molecule assays were conducted as described previously[32,33]. In brief, after purifying the proteins as described above, each motor was mixed with its corresponding IFT-B proteins in an equimolar ratio and incubated overnight at 4 °C in a rotator. To track the movement of the motor alone or in the presence of IFT-B proteins, microtubules were attached to the surface of a flow chamber (coated with 1 mg ml^{-1} biotinylated BSA and 1 mg ml^{-1} streptavidin (Sigma)) and the fluorescently labelled proteins were diluted to the desired concentration in BRB80 motility buffer (80 mM PIPES, pH 6.9, 10 mM ATP, 0.145 mg ml^{-1} glucose oxidase (Sigma), 0.0485 mg ml^{-1} catalase (Sigma), 20% glucose) and flowed into the chamber. Movement of the fluorescent signals was recorded with a cycle time of 235 ms with an objective-type Leica DMI6000 B TIRF microscope (Leica), equipped with a plan objective lens (100×, numerical aperture (NA) 1.47 oil), and a back-illuminated Andor U897 EMCCD camera (Andor). Excitation was achieved with the help of diode lasers at 488 and 635 nm wavelength, and frames were recorded and analysed with AF 6000 software (Leica). The velocities and run lengths were analysed with custom-written programs using MATLAB software (Mathworks). Spots were selected automatically according to their brightness compared with the mean brightness in each frame. The position of the spots was determined with subpixel accuracy using a radial centre approach. Runs were considered processive with a minimal run length of 1 μm. The run length data were fit to a truncated ($\chi_0 = 1$ μm) single-exponential distribution. Parts of the distance-over-time data were considered for speed calculation in a linear fit of at least six frames that resulted in a $r^2 > 95\%$. Landing events were counted from the data obtained using the tracking algorithm described above. Events that started after the first frame and showed a displacement from the binding position of at least 2 μm while associated with the microtubule were counted (n). As no processive movement was observed for the OSM-3–SNAP, runs were not selected for unidirectionality. Images of the microtubule positions were obtained from maximum intensity projections of the single molecule movies and their length (l) were measured using ImageJ. Considering the total length of a movie (t), the landing rate for a movie was calculated as $e = n/l/t$. This value was then corrected for relative dilution (c) of the motor over the motor plus adaptor) ($e_{corr} = e/c$). The mean of this value over three independent purifications was calculated alongside the s.d. and reported. For the colocalized movements, runs were compared pairwise from the two channels. Weighted penalties resulted from the mean distances of tracked positions (pixel, factor 1/3) and the difference of the starting time (frames, factor 1). Runs with a penalty below ten were considered and parameters are averages of single runs.

Colocalization assays. Proteins were mixed in equimolar concentrations, incubated overnight at 4 °C and flowed into chambers as described above for single-molecule assays. Fluorescence was detected using TIRF illumination. The colocalized images were analysed using custom-written routines in MATLAB software (MathWorks).

Reporting summary. Further information on experimental design is available in the Nature Research Reporting Summary linked to this paper.

Code availability. Custom-written codes used in this study are available from the corresponding author upon reasonable request.

Data availability. All data that support the findings of this study, including uncropped SDS–PAGE analyses of purified complexes, the detailed sequences of the motor constructs used in the study, are contained within the paper and its Supplementary Information or are available from the corresponding author upon reasonable request. Source Data for Figs. 2, 3 and Extended Data Figs. 4, 5, 7 are available with the online version of the paper.

32. Oberhofer, A. et al. Myosin Va's adaptor protein melanophilin enforces track selection on the microtubule and actin networks in vitro. *Proc. Natl Acad. Sci. USA* **114**, E4714–E4723 (2017).
33. Stepp, W. L., Merck, G., Mueller-Planitz, F. & Ökten, Z. Kinesin-2 motors adapt their stepping behavior for processive transport on axonemes and microtubules. *EMBO Rep.* **18**, 1947–1956 (2017).